

Entrainment induced by waves at a density interface impinged by a turbulent jet

J. Herault ^{1,2,†}, G. Facchini ², and M. Le Bars²

¹Institut de Radioprotection et de Sûreté Nucléaire (IRSN), 13115 St Paul lez Durance, France.

²Aix Marseille Univ, CNRS, Centrale Marseille, IRPHE, UMR 7342, 49 rue F. Joliot-Curie, 13013 Marseille, France

(Received xx; revised xx; accepted xx)

Using water/salty-water laboratory experiments, we investigate the mechanism of erosion by a turbulent jet impinging on a density interface, for moderate Reynolds and Froude numbers. Contrary to previous models involving baroclinic instabilities, we show that the entrainment is driven by interfacial gravity waves, which break and induce mixing. The waves are generated by the turbulent fluctuations of the jet and are amplified by a mechanism of wave-induced stress. Based on the physical observations, we introduce a scaling model which varies continuously from the Fr_i^3 to the Fr_i power law from small to large Froude numbers, in agreement with some of the previous laboratory data.

Key words:

1. Introduction

Turbulent mixing in stratified flows is found in many geophysical and industrial situations and relies on a complex process where the kinetic energy is irreversibly converted into potential energy (Fernando 1991; Fernando & Hunt 1996). The present paper considers the case of a sharp density interface impinged by a turbulent round jet. The turbulent jet of light fluid (water) of density ρ_1 impinges on a volume of denser fluid (salty water) of density $\rho_2 > \rho_1$, such that the outflow of the jet is orientated in the gravity direction \vec{g} and orthogonal to the density interface. The jet is driven by an upstream pump. The salty water is progressively mixed with the fresh water until the gradients of density disappear. In this process, two mechanisms can be identified: the entrainment and the mixing. The entrainment corresponds to the advection at the interface of dense fluid patches into the lighter fluid, where the flow is turbulent. The mixing consists in the thinning of the fluid patches by the turbulence until the spatial scale reaches the molecular diffusion scale, where both fluids are irreversibly mixed. The turbulent entrainment is quantified by the entrainment rate (Baines 1975)

$$E_i = \frac{Q_e}{\pi b_i^2 u_i} \quad (1.1)$$

where Q_e refers to the volumetric flux entrained across the interface and u_i and b_i correspond to the vertical velocity and the width of the jet at the interface. Baines (1975) suggested that for a turbulent flow, the entrainment rate E_i depends only on the interfacial Froude number, where the Froude number is $Fr_i = u_i/\sqrt{b_i g'}$ with $g' =$

† Email address for correspondence: herault@irphe.univ-mrs.fr

$g(\rho_2 - \rho_1)/\rho_1$ the reduced gravity acceleration. The Froude number characterizes the competition between the inertial force, which perturbs the interface, versus the restoring buoyancy force. Since Baines (1975), the entrainment flux has been commonly expressed as a power-law function of Fr_i with $E_i \propto Fr_i^n$ and $n \in [0, 3]$.

The significant scatter in measurements of the entrainment rate has been summarized by a recent review of Shrinivas & Hunt (2014) for jet, plumes and fountains. They report the entrainment rates of different studies (Baines 1975; Kumagai 1984; Baines *et al.* 1993; Lin & Linden 2005) and show that at low Froude number, two distinct trends are observed. The measurements of Linden (1973), Baines *et al.* (1993) and Lin & Linden (2005) for fountains and Baines (1975) for plumes follow approximatively the scaling law $E_i = 0.07Fr_i^3$ for $0.3 < Fr_i < 1.4$. The measurements of Kumagai (1984) for a plume display a distinct branch with larger entrainment rates. Kumagai (1984) originally characterized the scaling law by $E_i \propto Fr_i^3$ but Shrinivas & Hunt (2014) propose the scaling law $E_i = 0.24Fr_i^2$. Cotel *et al.* (1997) have also studied the entrainment rate for an impinging jet. They observed two different behaviours: a linear scaling with $E \propto Fr_i$ for $0.3 < Fr_i < 1$, which decays to a constant for $Fr_i < 0.14$. A universal law for the entrainment rate as a function of the solely Froude number seems to be ruled out by the previous experimental investigations, which suggest that other parameters must be taken into account.

Breidenthal (1992) and Cotel & Breidenthal (1996) proposed to characterize the regimes with the Reynolds numbers $Re = u_i b_i / \nu$, where ν is the kinematic viscosity, in addition to the Froude number. Baines (1975) showed that the entrainment rate does not depend on the Reynolds number providing the flow is turbulent. However, Shy (1995) observed that the properties of the flows inside the impinged region change drastically when the Reynolds number is increased. For moderate Reynolds number ($10^3 < Re < 10^4$), the density interface in the impinged region remains sharp with a small mixed layer thickness but above $Re \simeq 10^4$, the thickness of the density gradient increases by a factor 10 : it is the so-called mixing transition. Shy (1995) interpreted this transition as a strong enhancement of baroclinic turbulence inside the dome. Cotel *et al.* (1997) verified the presence of this transition, but the authors confirmed the experiments of Baines (1975) by showing that E_i remains independent of the Reynolds number for $Re \in [2200 - 12400]$. The problem of how the phenomenology differs at the transition without modifying E_i is still open.

Describing the turbulent flow as a superposition of vortices, the models of erosion are commonly based on the mixing capacity of vortices, determined by their Froude number $Fr_\lambda = u_\lambda / \sqrt{\lambda g'}$, with radius λ and velocity u_λ (Linden 1973; Shy 1995; Cotel *et al.* 1997; Cotel & Breidenthal 1996). Only the vortices with $Fr_\lambda > 1$ are expected to contribute significantly to the entrainment in the impinging region. The classical model of engulfment of Linden (1973) states that the eddies rebounding on the interface engulf the dense fluid before being advected by the mean flow outside the dome. Linden (1973) proposes a law $E_i \propto Fr_i^3$ based on scaling arguments and kinetic and potential energy balance. Shy (1995) and Cotel *et al.* (1997) report the presence of persistent baroclinic vortices localised around the periphery of the dome. The baroclinic vortices are generated by the incident small scales vortices advected by the turbulent jet. From these qualitative observations, Shrinivas & Hunt (2014) suggest a mechanism of entrainment based on a stationary circulation driven by like-sign vortices forced by baroclinic effects. For the low Froude number regime, it leads to a scaling $E_i \propto Fr_i^2$ in unconfined geometries. In confined geometries, Shrinivas & Hunt (2015) suggest that the presence of large scale oscillations of the interface leads to a correction Fr_i^3 , so that the entrainment rate becomes $E_i \sim Fr_i^2 + KFr_i^3$, with a constant K vanishing in the unconfined limit.

They show that the confinement effect may explain the scatter of the data observed in their (Fr_i, E_i) graphics, i.e. the existence of two branches at low Froude number.

The model of Shrinivas & Hunt (2015) attempts to rationalise the different entrainment laws but it relies on the presence of vortices driven by baroclinic forces, even if no experimental study has demonstrated quantitatively their existence. The presence of the mixing transition suggests that the strength of the baroclinic vortices inside the dome depends on the Reynolds number of the turbulent jet. Turbulence in jets with large Reynolds numbers ($Re > 10^4$) is expected to be developed and to display small scales structures, more efficient to generate baroclinic (Shy 1995), whereas jets with moderate Reynolds numbers ($10^3 < Re < 10^4$) remain dominated by large scale structures (Dimotakis 2000). These points raise two questions: can the vortices of a turbulent jet drive baroclinic eddies for Reynolds numbers below the mixing transition? What is the mechanism of entrainment at moderate Reynolds numbers if the baroclinic vortices are absent? These questions will be addressed here.

In the present paper, we aim at determining the mechanism of entrainment of a non-buoyant jet impinging a sharp density interface via velocity and density measurements for Reynolds numbers below the mixing transition. Our experimental set-up is presented in section 2 and 3. Our study holds for moderate Fr_i , i.e. $Fr_i < 1$, corresponding to a relatively small deformation of the interface, and for moderate Reynolds numbers ($Re \simeq 2 \times 10^3$). Our measurements support a mechanism where the entrainment is driven by interfacial gravity-waves as shown in section 4. The waves are generated by incident vortices and amplified during their propagation outside the impinging region. This amplification leads to wave breaking associated with local mixing. Based on our measurements and on this mechanism, we introduce in section 5 a model describing the continuous change of the scaling law for turbulent entrainment from small to large Froude number.

2. Experimental set-up

2.1. Set-up and measurements

The set-up is sketched in figure 1(a). The tank is rectangular with a square section of width $L = 30$ cm and height $H = 50$ cm. The tank is filled with one layer of light fluid of density ρ_1 and height $h_1 = 25$ cm above a layer of denser fluid of density ρ_2 and height $h_2 = 14$ cm (figure 1). The densities are controlled by a density meter DMA 35 from Anton Paar. The upper part of the tank is filled with water, plus some ethanol for the experiments indexed by M1, M2 and M3 in table 1. The lower part of the tank is filled with a saline solution of density ρ_2 . The solution of ethanol in the light fluid allows us to match the optical index of the saline solution below. The viscosity of the mixture water plus ethanol is a non-linear function of the percentage of ethanol. The index matching is performed for density jump $\Delta\rho \simeq 0.03\text{g/cm}^3$. The measurements are performed with an initial density $\rho_1 = 0.987$, which is associated with a kinematic viscosity of $\nu = 1.2 \times 10^{-6}\text{m}^2/\text{s}$ at 298K (Khatab *et al.* 2012). The initial viscosity is 22% larger than the viscosity of the water but the mixing will progressively decrease this difference during the run. All the fluids are freshly prepared for each run and filtered (20 microns filter). The velocity of injection U_{inj} at the round nozzle of radius $b_0 = 0.2$ cm is fixed for each experiment. The pump for the injection is located in one of the upper corner of the tank: the experiments are thus performed with a constant volume. Our measurements shows that the pumping system does not modify significantly the symmetries and properties of the mean velocity field.

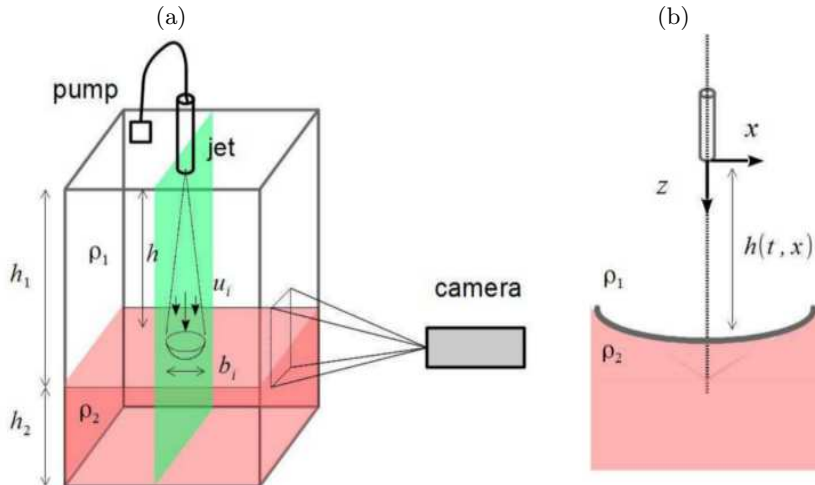


FIGURE 1. (a) A schematic of the experimental set-up showing a rectangular tank filled with water (h_1) and a saline solution (h_2). The nozzle is located at a height $h_0 = h(x = 0, t = 0)$ from the interface. (b) We define the reference frame (x, z) associated with the nozzle. The z direction is descending.

Run	U_{inj} [m/s]	$\Delta\rho$ [g/cm ³]	h_0 [cm]	Fr_{inj}	Re	Fr_i	b_d [cm]	ξ [cm]
T1	1.15	—	—	—	2.3×10^3	—	—	—
M1	1.03	0.031	24	41.8	2.0×10^3	0.56	4.0	2.0
M2	1.15	0.031	24	46.6	2.3×10^3	0.63	3.4	0.8
M3	1.15	0.028	24	49.1	2.3×10^3	0.66	4.0	1.5

TABLE 1. Experimental parameters for the 4 conducted experiments.

Two different experimental investigations are performed: the first one for the description of the turbulent jet without density variation, and the second one for the investigation of the mixing mechanism. The runs are respectively indexed by “T” and “M”(table 1). The physical properties of the waves (section 4.2) and the features of the breaking (section 4.5) are determined from the measurements of the density field, run indexed by M2. The excitation (section 4.3) and the amplification (section 4.4) of the waves are mostly characterized by the velocity measurements in runs indexed M1 and M3. We have checked that the runs display the same features, like the signature of the wave period in the measurements of density M2 (figure 9) and in the measurements of velocity M1 (figure 11(a)). The measurements start four minutes after the beginning of the erosion. We performed both velocity and density measurements using a digital camera (FASTCAM Mini, Photron) with a spatial resolution of 1024×1280 pixels.

The velocity field is measured in the experiments T1, M1 and M3, using the particle image velocimetry (PIV) process (Meunier & Leweke 2003). The flow is seeded with tracer particles ($< 10\mu\text{m}$) and it is illuminated by a laser sheet crossing the vertical plane of the jet. The dimensions of the interrogation windows are 15×20 cm². The acquisition rate is performed at 125 fps and 5000 frames are acquired. The PIV algorithm is based on a first 64×64 pixels and a second 32×32 pixels interrogation regions, and the resulting velocity field is a 64×72 vector field. The convergence of the mean field is insured for

an ensemble of frames larger than 4000 snapshots. During the PIV measurements, the interface between the fluids is detected independently via a small amount of rhodamine in the dense fluid. In the experiment M2, the density is measured by a planar laser-induced fluorescence technique (PLIF) with the same laser and camera set-up. The saline solution is mixed with rhodamine B. This rhodamine has an absorption spectrum between 460 and 590 nm and its emission spectrum is 550-680 nm, well separated from the laser light. A high-pass filter (TIFFEN Filer, orange 21) is mounted on the camera with a cut off frequency of 550nm. The calibration has been performed with uniform fields of density. The dye concentration has been adjusted to have a linear relation between dye concentration and intensity. From this calibration process, we have calculated the measured spatial intensity distribution, called also flat-field, which takes into account the biased of intensity due to the lighting inhomogeneity or the camera response. The density of rhodamine is then calculated from the intensity field corrected by the flat-field. Here, we are only interested in iso-density contours defining the interface. We define the interface height $h(x, t)$ as the curve of iso-density $\rho = (\rho_1 + \rho_2)/2$.

The initial distance between the end of the nozzle and the interface is $h(x = 0, t = 0) = 24$ cm (runs M , see table 1), i.e. 60 times the diameter of the nozzle in order to obtain a developed turbulent jet (List 1982). To describe the flow, we use the frame in the plane of symmetry of the jet (figure 1(b)) with the cartesian coordinate system (x, z) . The x -axis is aligned with the radial direction and the z -axis corresponds to the axis of symmetry of the jet. The origin is located at the nozzle outlet. Due to the axisymmetry of the configuration, we assume that the time-averaged quantity of the azimuthal component of the velocity fields, here in the y direction, and the derivative of the average quantities with respect to y , are equal to zero. The measurements performed in the vicinity of the impinged region are expressed as a function of the radial distance x and the distance from the interface $h_0 - z$, where $h_0 = \langle h(x = 0) \rangle$ is the time average distance from the nozzle to the interface along the axis of the jet.

2.2. Interfacial dimensionless parameters

In table 1, we report the Froude numbers and the Reynolds numbers associated with the jet for each run: $Fr_{inj} = U_{inj}/\sqrt{b_0 g'}$ and $Re = U_{inj} b_0/\nu$. The Reynolds number is expected to be constant in the far field of the jet (List 1982). The Reynolds numbers are between 2×10^3 and 2.3×10^3 , which implies that our experiments are below the mixing transition (Shy 1995), where the mixing layer thickness is small. We investigate the properties of the solely turbulent jet configuration in the next section. From the Froude numbers Fr_{inj} , we calculate a relevant Froude number at the interface Fr_i by interpolating the typical length b_i and velocity u_i at the interface. We use the classical law of evolution of the width of the jet b and the axial velocity component u_m with a distance z from the nozzle (Fischer *et al.* 1979)

$$b(z) = \frac{db}{dz}(z - h_s) \quad \text{and} \quad u_m(z) = U_{inj} \Lambda \frac{2b_0}{(z - h_s)} \quad (2.1)$$

with (db/dz) the spreading rate, Λ the velocity decay constant and h_s the virtual origin of the jet reported in table 2.2. We use the top-hat definition for the typical length b_i and velocity u_i . The top-hat definition for a gaussian profile allows us to define $u_i = u_m(h)/2$ and $b_i = b(h)$ with h the position of the interface. The recent numerical experiment of Ezhova *et al.* (2016) supports the use of equations (2.1) showing that the axial velocity component u_m (Fig.6(a)) is modified only in the near field of the interface. The Froude number at the interface

	$b_0[\text{cm}]$	Re	$z/(2b_0)$	$h_s/(2b_0)$	(db/dz)	Λ
T1	0.2	2.3×10^3	40 – 85	2.29	0.096	5.51
Hussein <i>et al.</i> (1994)	1.27	47.7×10^3	16 – 96	4	0.093	5.9

TABLE 2. Parameters of the turbulent jet compared to the measurements of Hussein *et al.* (1994).

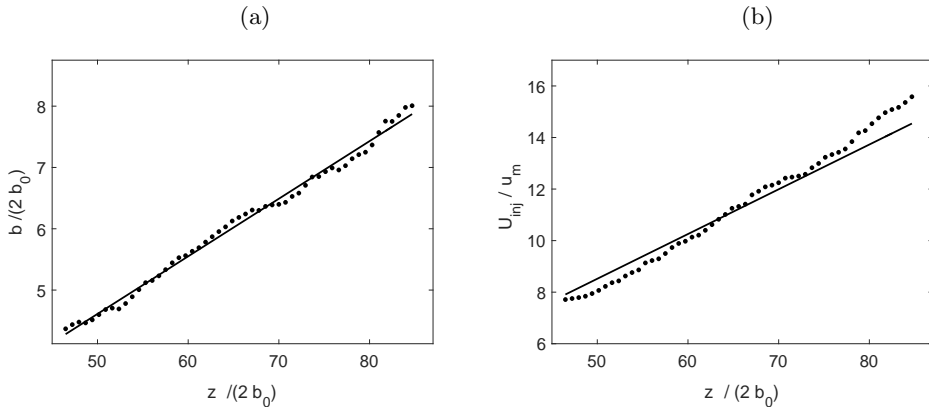


FIGURE 2. (a) Radius b of the jet and (b) inverse of the axial velocity u_m as a function of the distance from the nozzle z rescaled by the diameter of the nozzle $2b_0$.

$$Fr_i = \frac{u_i}{\sqrt{b_i g'}} \quad (2.2)$$

writes as a function of the position of the interface h

$$Fr_i = Fr_{inj} \frac{\Lambda}{(db/dz)^{1/2}} \left(\frac{b_0}{h - h_s} \right)^{3/2} \quad (2.3)$$

Thus the Froude number decreases like $Fr_i \sim h^{-3/2}$. Our study is performed during a limited duration after the initial transient and, it is reasonable to consider that the Froude number has not varied significantly since the beginning of the experiment.

3. Kinematics of the jet

3.1. Jet without stratification

We first study the jet in the absence of stratification for a Reynolds number $Re = 2.3 \times 10^3$ (T1 in table 1) in order to validate the use of equation (2.1). The measurements are performed for z between $80b_0$ and $170b_0$. The local radius of the jet b divided by the diameter $2b_0$ is reported as a function of $z/(2b_0)$ in figure 2(a). The radius b corresponds to the ordinate x where the average vertical velocity corresponds to the half of the axial velocity, i.e. $\langle u_z \rangle(x, z) = u_m(z)/2$, for a given z . The radius increases linearly and the fitted parameters $(db/dz, h_s)$ (equation (2.1)) are reported in table 2. The ratio $U_{inj}/u_m(z)$ (figure 2(b)) increases also linearly and the corresponding parameter Λ is

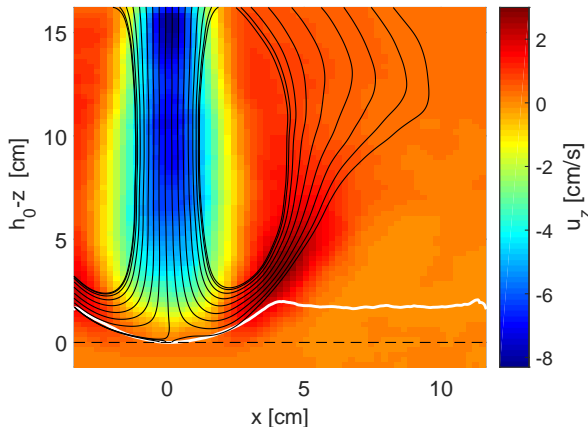


FIGURE 3. Streamlines (black curves) of the mean flow, superimposed on the vertical component of the mean velocity field $\langle u_z \rangle$ (cm/s) (colorbar). The white curve corresponds to the time-averaged location of the interface separating both fluids. The black dotted line corresponds to the ordinate $h_0 - z = 0$.

reported in table 2. The coefficient Λ is fitted by taking $u_m(z)$ as a function of $z - h_s$ with h_s obtained from the data of figure 2(a). The measured coefficients ($h_s, db/dz, \Lambda$) are compared to the results of Hussein *et al.* (1994) for $Re = 47.7 \times 10^3$, based on the radius of the nozzle. Our measurements are in good agreement, regarding db/dz and Λ , which are related to the physics of the mixing by the turbulent jet: this validates the use of Taylor entrainment constant. The virtual origin is different but it depends strongly on the range of fitting z/b_0 , as demonstrated by Wygnanski & Fiedler (1969).

3.2. Jet with stratification

We now focus on the velocity field of a jet impinging on a sharp density interface. The results presented here correspond to the run M1 (table 1). The vertical component $\langle u_z \rangle$ of the time-averaged velocity field and its streamlines are reported on figure 3. The operator $\langle \cdot \rangle$ corresponds to the time-averaged quantities calculated on a duration $T_e = 40$ s corresponding approximately to 100 advection time scales b_i/u_i . The white curve represents the time-averaged location of the interface determined by the presence of fluorescent rhodamine. The vertical axis at $x = 0$ corresponds to the jet axis and the height $h_0 - z = 0$ is associated with the bottom of the time-averaged interface (black dashed line).

We have reported in table 1, the depth and the radius of the time-averaged dome generated by the impact of the jet on the stratified interface for M1, M2 and M3. The radius b_d is the radial distance between the center of the dome (almost parabolic) and the end of the dome, where the interface becomes flat. The depth ξ corresponds to the difference of altitude between these two extremities. For M1, the dome is characterized by a radius $b_d = 4$ cm and a depth $\xi = 2$ cm. The abscissa x and the height z will be rescaled respectively by b_d and ξ in the rest of the paper. The radius of the jet at the interface b_i , equal to 2.2cm, corresponds approximately to the width of the jet entering in the dome and it is approximately two times smaller than the radius of the dome.

A remarkable property of the flow inside the dome is the convergence of the streamlines leaving the dome close to the interface. This contraction corresponds to a local acceleration of the flow. To study the flow field inside the dome, we introduce the

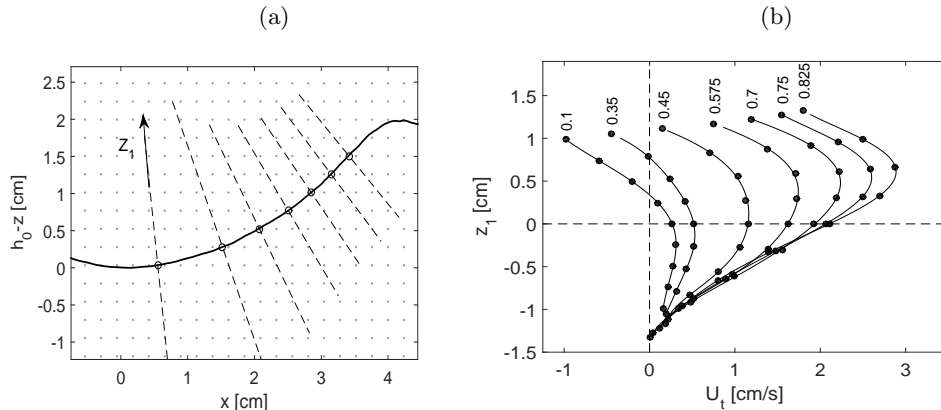


FIGURE 4. (a) Location of the points on the interface with the normal line (dashed line) where the tangential velocity U_t is calculated. (b) The profiles of U_t are calculated at the abscissa $x = 0.1, 0.35, 0.475, 0.575, 0.7, 0.775, 0.825$ times the radius of the dome b_d . The variable z_1 is the distance from the interface following the dashed curves in (a).

velocity component U_t , which is tangential to the mean interface given by the function $\langle h(x, t) \rangle$. For each abscissa x , we calculate the angle of inclination of the interface given by $\theta(x) = \arctan(d\langle h \rangle/dx)$ and we define the velocity by $U_t(x, z) = \sin(\theta)\langle u_z \rangle + \cos(\theta)\langle u_x \rangle$. The profiles of U_t are reported in figure 4(b) for different abscissae shown in figure 4(a) (from left to right) starting at $x = 0.4\text{cm}$ ($0.1b_d$) and finishing at 3.3cm ($0.825b_d$). They are plotted as a function of the ordinate z_1 following the normal to the interface (dashed lines in figure 4(a)) with the interface at $z_1 = 0$. The curves correspond to the polynomial interpolation of the profiles. The profiles confirm that the flow accelerates along the interface.

A balance between potential energy and kinetic energy explains the acceleration characterized by $\partial_x U_t > 0$. When the jet impacts the interface, the kinetic energy is converted partially into potential energy. When the flow leaves the dome, a part of the potential energy is reconverted into kinetic energy. We have calculated the kinetic energy $E_c = (\langle u_x \rangle^2 + \langle u_z \rangle^2)/2$ as a function of the height z along the interface (figure 5(a)). The kinetic energy increases initially linearly with the height z until $z \simeq 0.6\xi$, which corresponds to the abscissae $x \simeq 0.8b_d$. The time-averaged interface follows the streamline of the time-averaged flow passing close to the stagnation point at $(x, z) = (0, 0)$. Shrinivas & Hunt (2014) (equation (3.9)) suggest that despite the presence of turbulence, the Bernoulli equation can be applied along the streamline following the interface. By assuming a pressure balance at the interface and a vanishing velocity below the interface, they obtain $E_c = g'z$. However, our measurements show that the kinetic energy follows $E_c = (0.06g'z)$: only six percent of the potential energy is transferred into kinetic energy. The application of the Bernoulli equation breaks because the velocity does not vanish rapidly below the interface (figure 4(b)) and it considers neither the process of entrainment nor the turbulent fluctuations, which must consume an important part of the potential energy. Outside the dome, the streamlines are directed upward and reconnect the jet flow drawing a large recirculation cell. This recirculation is the combination of the ballistic reflection of the jet and the lateral entrainment of the jet.

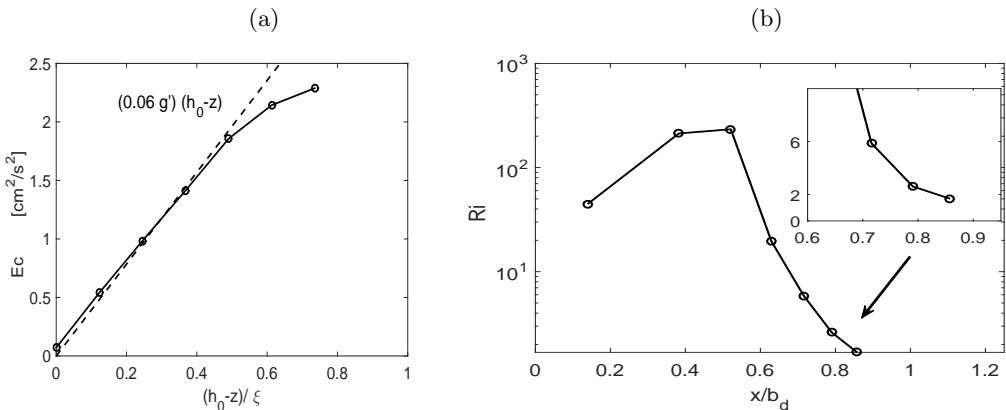


FIGURE 5. (a) Kinetic energy E_c as a function of the height along the interface. (b) Richardson number as a function of x/b_d with $Ri = (g'/b_d)/s_0^2$ and $s_0 = (\partial_{z_1} U_t)_{z_1=0}$.

4. Investigation of the mechanism of erosion

4.1. General description

We first draw a global picture of the mechanism of erosion before demonstrating each element in the following paragraphs. When the jet impinges on the dense fluid, the interface is convoluted by the turbulent fluctuations of the jet. These perturbations are generated by eddies coming from the jet. These vortices excite interfacial gravity waves propagating outward the impinged region (figures 6). During the propagation, the height of the waves increases until they breakdown close to the border of the dome. This process is illustrated on the three successive pictures of the interface of figure 6(b), with waves propagating from left to right. The amplification of the waves is caused by an energy transfer from the mean flow via a mechanism, which could be similar to the one described by Miles (1960) in shear flows. The breaking of the waves induces a strong mixing due to the wrapping of filaments. The heavy fluid is then transported in the bulk flow where the turbulence of the jet mixes both fluids (figure 6(a)). We claim that the transport and the mixing of the dense fluid by these waves is the main source of erosion at low Froude number and moderate Reynolds numbers. The following sections detail successively the former points.

4.2. Wave properties

In this section, we characterize the properties of the perturbations near the interface. We observe that the interface remains sharp in the impinged region, as expected for $Re < 10^4$ (Shy 1995) with a small diffusion layer δ_H . The height of δ_H corresponds to few percent of the dome depth, i.e. few millimeters. The stratification in this layer could support internal gravity waves with typical frequency $N = \sqrt{g'/\delta_H}$ with $\Delta\rho/\delta_H$ the associated density gradient. The frequency of internal gravity waves would be $N \simeq 8\text{Hz}$ for $\delta_H \simeq 4\text{mm}$. As we will see further, the typical frequency of the waves propagating inside the dome varies in the range $0.3 - 0.4$ Hz, a frequency range corresponding to interfacial gravity waves. Hence, the dynamics of the perturbation inside the dome is controlled by interfacial gravity wave rather than internal gravity wave.

The spatio-temporal properties of the waves is studied by using the information contained in the dynamics of the interface. The perturbation of the interface is illustrated by an instantaneous relative density field from the measurement M2 (figure 7). The relative density is defined by $\hat{\rho} = (\rho - \rho_1)/(\rho_2 - \rho_1)$ varying between 0 and 1, with ρ

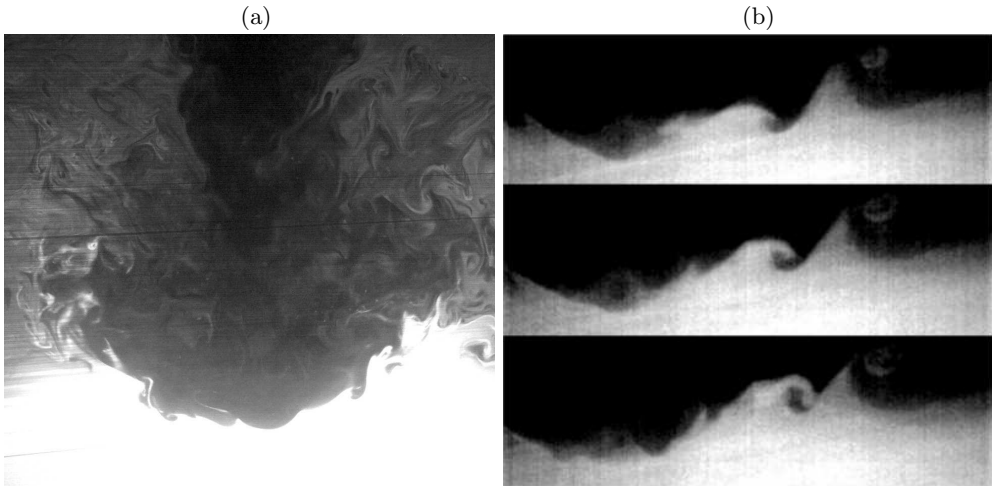


FIGURE 6. (a) Mixing process in the vicinity of the interface ($15 \times 20\text{cm}^2$) and (b) of the dome head ($15 \times 8\text{cm}^2$). The dense fluid has been dyed by rhodamine and corresponds to the bright region. See online supplementary material (movie1) for the movie corresponding to figure (a).

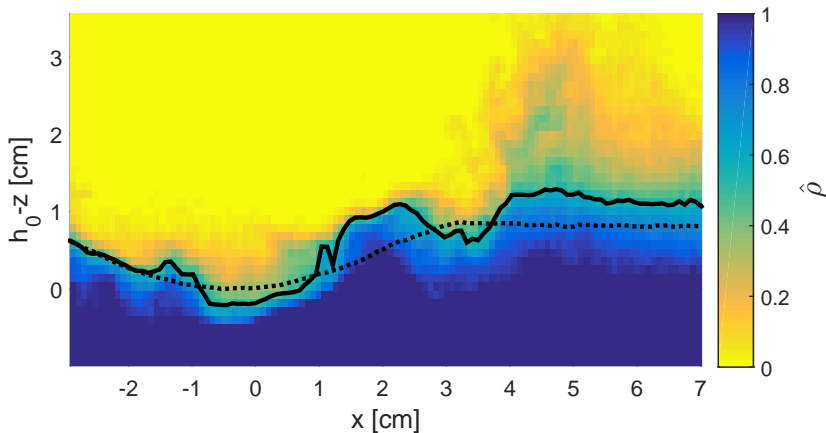


FIGURE 7. Rescaled density field $\hat{\rho}$ (colour level) from $\hat{\rho} = 0$ for $\rho = \rho_1$ (fresh water) to $\hat{\rho} = 1$ for $\rho = \rho_2$ (initial salty water). The heavy black curve corresponds to the height $h(x, t)$ where $\hat{\rho} = 0.5$. The dashed curve represents the time-averaged height $\langle h \rangle$.

the effective density given by the LIF measurements. The interface position defined by $h(x, t)$ (black curve) corresponds to the iso-density line $\hat{\rho} = 0.5$. The time-averaged height $\langle h \rangle(x)$ is represented by a black dotted curve following a quadratic law $\langle h \rangle \sim x^2$ in the impinged region.

From the height $h(x, t)$, we introduce the height perturbation $\eta(x, t) = h(x, t) - \langle h \rangle$ and we perform a two-dimensional spectrum of the spatio-temporal evolution of $\eta(x, t)$. It consists in projecting the spatio-temporal field $\eta(x, t)$ inside the dome, i.e. $|x| < b_d$, on the 2D Fourier space (k, F) . We restrict the spatial domain to the dome region, where the waves are generated and amplified. We report in figure 8, the two-dimensional power-spectrum with frequencies below 0.6 Hz and wavenumbers smaller or equal to $2k_0$, with $k_0 = 2\pi/b_d$ (run M2, table 1). This bandwidth contains 89 percent of the total energy. The temporal dynamic of the height η is mostly modulated by two time-spectral components:

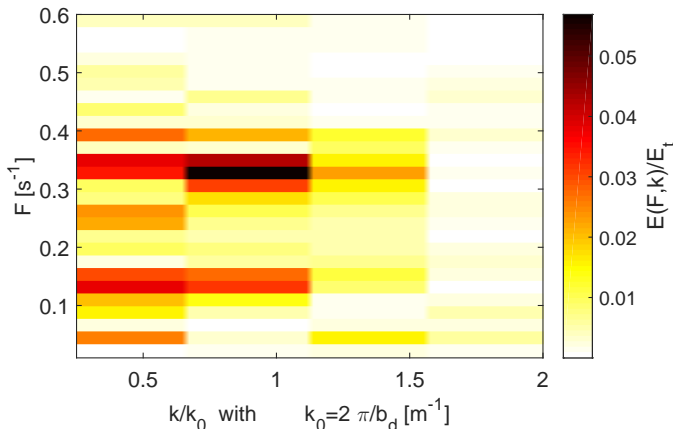


FIGURE 8. Two-dimensional power-spectrum $E(k, F)$ of the elevation $\eta(x, t)$. The wave number k is rescaled by $k_0 = 2\pi/b_d$ and the density of energy is rescaled by the total energy E_t .

slow standing modes and interfacial gravity waves. The slow mode is characterized by frequencies in the range $F \in [0.05 - 0.15]Hz$ with a peak in the mode with wavelength $k = 0.5k_0$. The waves are characterized by wavenumbers between $0.5k_0$ and k_0 , i.e wavelengths between b_d and $2b_d$, and frequencies in the range $F \in [0.3 - 0.4]Hz$, i.e a typical period with $T = 2.9 \pm 0.4s$. The energy in the waves is approximatively two times larger than the energy in the slow modes. The precise characterization of the wavelength is difficult because the wavelength is comparable with the length of propagation. The dispersion relation of interfacial waves for irrotationnal flow gives a period of $2\pi(k_0gAt)^{-0.5} \simeq 1.85s$, a value comparable to the measured one. The difference may be explained by the presence of an inclined interface of propagation or by the Doppler shift associated with a mean non-uniform flow.

By using a bandpass filter containing the frequency range $[0.3 - 0.4]Hz$, we are able to extract the propagation of the interfacial waves. The spatio-temporal diagram of the bandpass filtered η is reported on figure 9(a), with the abscissae rescaled by b_d and the time t by the period of the waves T . The amplitude η of the waves is divided by the depth of the dome ξ . The spatio-temporal diagram displays wave patterns with a half-wavelength comparable to the dome radius. The wave dynamic is complex but we observe that most of the waves propagates outward the dome, as illustrated by the figure 9(b). From the bandpass filtered elevation $\eta(x, t)$, we perform a lagrangian tracking of the waves, which consists in following the wave envelop. We report some trajectories $x(t)$ on figure 10(a) and calculate the phase velocity $c = \dot{x}(t)$. The velocities being not constant, we calculate the probability density function $p(c)$ of c for all the trajectories (insert of figure 10(a)). The distribution exhibits a maximum at $c_p = 2cm/s$, which will be taken as the reference phase velocity at the interface. The grey dashed curve on figure 10(a) corresponds to a trajectory with $x = c_p t + x_0$.

We also calculate the root mean square amplitude of the wave

$$A_\eta(x) = \sqrt{2} \left[\frac{1}{T_e} \int_0^{T_e} \eta^2(x, t) dt \right]^{1/2} \quad (4.1)$$

with the height perturbation η without the slow modes component suppressed by a high-pass filter and T_e the duration of the measurement. We report A_η (upper dotted

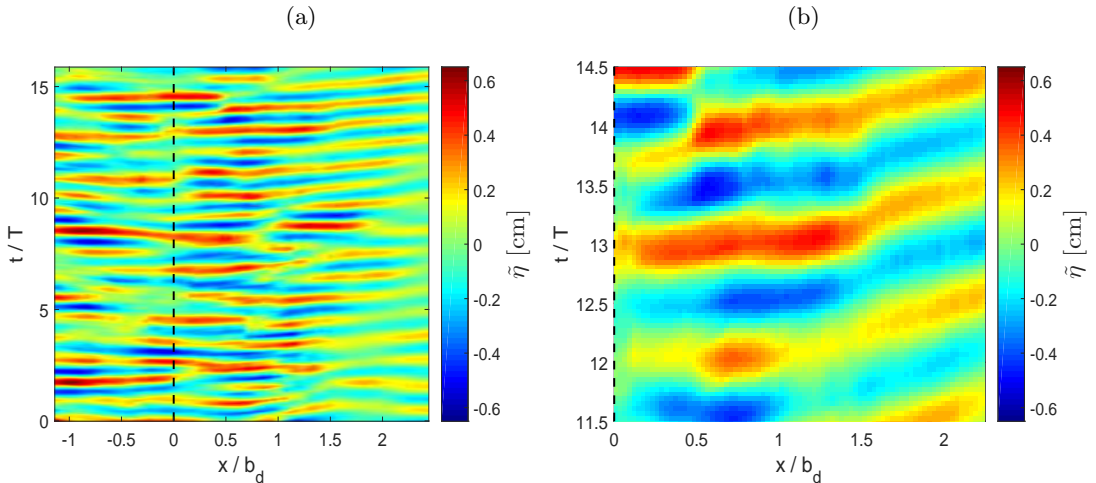


FIGURE 9. (a) Spatiotemporal diagram of the height perturbation $\eta(x, t) = h(x, t) - \langle h \rangle$, filtered in the frequency range $f \in [0.3 - 0.4]$ Hz. The abscissae are rescaled by the radius of the dome b_d , the time by the mean wave period $T = 2.9$ s and, the amplitude of the height by the depth of the dome ξ . (b) Zoom on the region $x \in [0 - 2.25]b_d$ and $t \in [11.5 - 14.5]T$.

curve, called total) as a function of x/b_d on the figure 10(b). The dashed curve (called fundamental) corresponds to the amplitude of the waves in the frequency range $[0.3 - 0.4]$ Hz (by using a band-pass filter) and the heavy curve corresponds to the amplitude with higher frequencies. Despite the fact that the typical length scale of the waves is comparable with the distance of propagation, we distinguish different behaviors of the amplitude of the wave during the propagation. We have reported the three regions of interest: the region I, where the waves are generated and amplified; the region II, where the waves break, and the region III out of the dome. The amplitude of the fundamental frequency increases in the region I ($|x| < 0.565b_d$), suddenly drops in the region II, and then decreases monotonically out of the dome $|x| > b_d$. In the breaking region, the amplitude of the modes with large frequencies decreases just after those of the fundamentals. The shift of the amplitude drop is a consequence of the wave breaking, where the density patches are wrapped and thinned (figure 6(b)).

4.3. Wave generation

We now focus on the waves excitation mechanism, with two possible candidates: the instability of the interface and the interface excitation by turbulent fluctuations. First, we investigate the stability of the interface and we demonstrate that the shear at the interface is not strong enough to trigger Kelvin-Helmholtz and Holmboe instabilities.

The stability of the interface is related to the local Richardson number given by $Ri = N^2/s_0^2$ with s_0 the shear defined by $s_0 = (\partial_{z_1} U_t)$ at $z_1 = 0$ and N the frequency of interfacial gravity waves. It compares the destabilizing effect of the shear to the stabilizing buoyant effects. The perturbations being interfacial gravity waves, the Richardson number is defined by $Ri = (g'/b_d)/s_0^2$ (Chandrasekhar 1961). It is worth noting that by using the frequency of internal gravity waves instead of the one of interfacial waves, the Richardson number becomes one order of magnitude larger than the one defined here.

The shear s_0 is calculated from the mean velocity field and corresponds to the tangential velocity gradient at the interface $\langle h \rangle$ (figure 4(b)). We have shown that the interface merges with a streamline of the average flow passing close to the stagnation point (figure 3). The mean velocity field along the interface satisfies the relation $\langle u_x \rangle \partial_x \langle h \rangle \simeq$

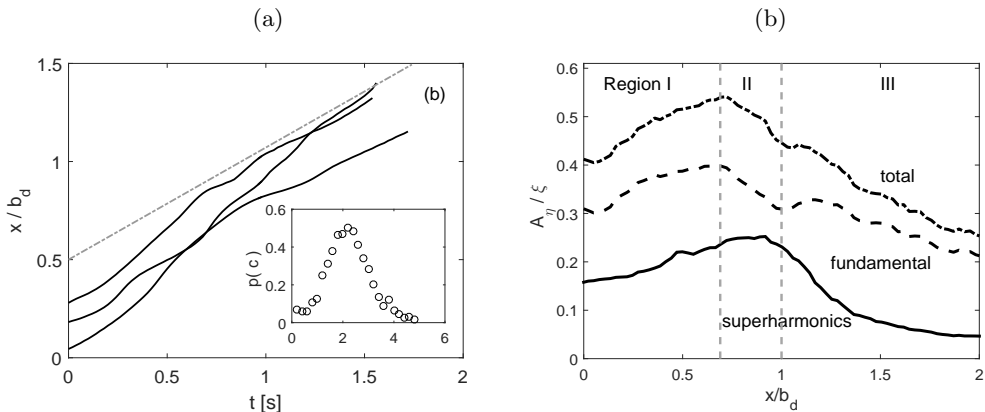


FIGURE 10. (a) Three trajectories of the wave envelop (heavy lines), compared to a virtual trajectory (dashed line) with constant phase velocity $c_p = 2$ cm/s. In the insert: distribution of the measured instantaneous phase velocity c . (b) Amplitude of the wave A_n given by (4.1). From top to bottom, the three curves show the total amplitude of the waves, the fundamental component and the higher harmonics.

$\langle u_z \rangle$ for $|x| < 0.6b_d$, which implies that $\partial_t \langle h \rangle \simeq 0$ by considering the continuity of the mean material line. The average velocity field and the mean position of the interface may be considered in quasi-equilibrium, supporting the stability analysis of the interface from the mean fields.

The local Richardson number is reported on the figure 5(b). It varies between 40 and 230 in the vicinity of the head of the dome, i.e. $|x| < 2.5$ cm or $0.61b_d$. It turns out that the interface should not be destabilized in this region by a classical Kelvin-Helmholtz instability operating for $Ri < 1/4$ (Miles 1961; Chandrasekhar 1961) (see also the numerical simulations by Woodward *et al.* (2014) on a closely related problem). We point out that the presence of a curved interface and an accelerating flow, i.e. $\partial_x U_t > 0$, may change the criteria of stability. Nonetheless these effects are only significant on the sides of the dome, where the waves are already excited and amplified.

Moreover, the length scale of the instability is not compatible with the one of the Kelvin-Helmholtz instability. For a sharp velocity jump, the smallest unstable wave number is given by (Chandrasekhar 1961)

$$k_{min} \simeq \frac{2gAt}{\Delta U^2} \quad (4.2)$$

with ΔU the velocity jump at the interface and $At = (\rho_2 - \rho_1)/(\rho_2 + \rho_1)$ the Atwood number. From figure 4(b), the largest velocity jump is typically $\Delta U_{max} = 1$ cm/s inside the dome. The numerical application gives $k_{min} = 5.8 \times 10^3$ m⁻¹ corresponding to a wavelength smaller than 0.1 cm. The Kelvin-Helmholtz instability could only trigger perturbations at scales 20 – 40 times smaller than the one observed. Reciprocally, the velocity jump should be at least 6 times larger to account for the observed wavelength. During the erosion process, Ri decreases (Kumagai 1984): if the interface is initially stable for the Kelvin-Helmholtz instabilities, it remains so during the erosion process.

An other alternative to the Kelvin-Helmholtz instability is the Holmboe instability (Holmboe 1962). This instability can operate for large Richardson numbers and Alexakis (2009) showed that it may appear for $Ri = 30$ (far from the 1/4 of the K-H instability). However, the Richardson number is larger than 40 for $|x/b_d| < 0.6$ in the dome. The mode associated with the Holmboe instability is also characterized by symmetric cusps at

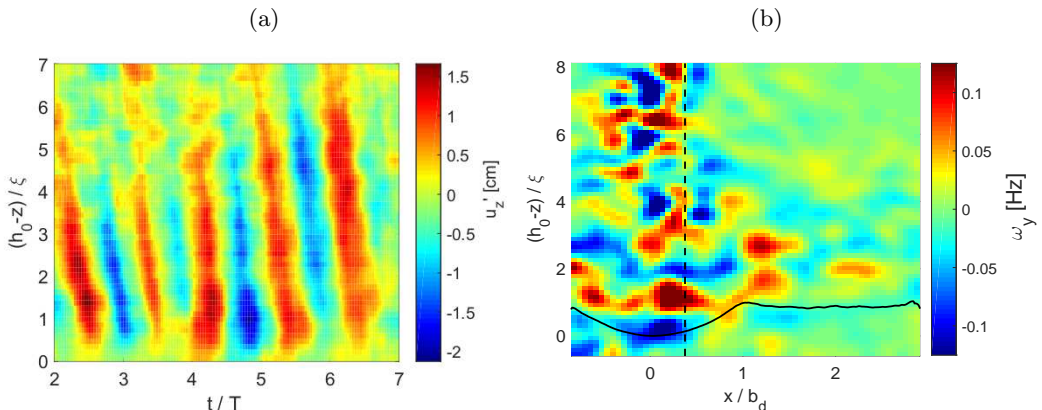


FIGURE 11. (a) Spatiotemporal diagram of the fluctuations u'_z in the range of frequencies $[0.3, 0.4]$ Hz along the vertical axis $x = 0.37b_d$. (b) Bandpass filtered fluctuations of the vorticity field, calculated from a coarse-grained velocity field with width of 0.75cm (Gaussian filter). The dashed curve represents the vertical axis at $x = 0.37b_d$.

large Richardson number (Strang & Fernando 2001). This pattern has not been observed in our experiment. We conclude that neither the Kelvin-Helmholtz instability nor the Holmboe instability generate perturbations on the interface.

The source of waves is ensured by the turbulent fluctuations of the jet. Having identified the region and the frequency range of the waves in section 4.2, we look for their signature in the turbulent jet. In order to demonstrate that the perturbations come from the jet, we focus on the fluctuations of the vertical velocity fluctuation $u'_z = u_z - \langle u_z \rangle$ along the axis $x = 0.37b_d$, represented by the dashed curve on figure 11(b). We calculate the bandpass filtered component of u'_z in the frequency range $[0.3 - 0.4]$ Hz. The associated spatio-temporal diagram is reported on the figure 11(a) with t and z rescaled by the period of the wave T and the depth of the dome ξ . We clearly identify perturbations propagating from the jet to the dome. It is worth noting that these fluctuations appear far from the dome at $|h_0 - z| \simeq (5 \pm 1)\xi$ and seem to be incoherent before. This region is far from the transitional distance close to the nozzle of the jet ($z < 50b_0$), where coherent structures may be generated in the early development of the jet (Yule 1978). Thus, it is possible that a coherent process, based on the interplay between the jet and the interface, may filter or select the perturbations far from the interface. The bandpass filtered fluctuation of vorticity field, calculated from a coarse-grained velocity field, is reported on figure 11(b) for a given time t . The fluctuations u'_z are associated with large scale vortices, which propagate toward the interface. The diameter of the vortices close to the dome is varying around $\lambda = 3 \pm 1\text{cm}$. At the entrance of the dome, the typical vertical velocity is $\langle u_z \rangle \simeq 2 \pm 1\text{cm/s}$ (figure 3). So a typical period of excitation corresponds to the advection of two vortices of opposite sign and the associated time scale of forcing is $2\lambda / \langle u_z \rangle \simeq 3\text{s}$, a value very close to the wave-period T .

From the fluctuation u'_z , we can estimate a Richardson number for the observed eddies. The maximum amplitude of u'_z reaches typical value given by $u_{max} = 2\text{cm/s}$. The Richardson number of these eddies is defined by $Ri_\lambda = g'\lambda / (u_{max}^2)$ (Cotel & Breidenthal 1996) and corresponds to $Ri_\lambda \simeq 22$. An energy balance between the kinetic energy of the vortex and the potential energy associated with the penetration depth δ gives $\delta / \lambda \sim Ri_\lambda^{-1}$ (Linden 1973). From the measured Richardson number, the penetration depth is of order $\delta / \lambda \simeq 10^{-2}$. Thus the convolution of the interface is expected to be too small if we consider the classical model of the vortex impact. It has been recently demonstrated in

the context of internal-gravity waves excited by turbulent plume that waves can be forced by the bulk pressure-field of the turbulence (Lecoanet *et al.* 2015). This approach could be fruitful to explain the wave excitation for eddies with low Richardson numbers.

4.4. Wave amplification

The observed growth of the perturbations along the interface (figure 10(b)) may be explained by a mechanism of wave amplification. Furthermore, the axisymmetry of the configuration leads a priori to a decrease of the energy of the perturbations, due to the radial spreading of the energy. Thus, the amplification must at least counterbalance the energy spreading due to the axisymmetry. As shown in the previous section, the amplification mechanism could not be explained by the Kelvin-Helmholtz and Holmboe instabilities. It is interesting to note that our configuration shows some similarities with the problem of the generation of ocean-waves by turbulent wind (Janssen 2004). The ocean-waves are generated by turbulent pressure fluctuations with a sheared mean flow. Like in our configuration, the Kelvin-Helmholtz is not the best candidate to explain the generation of ocean-waves (Janssen 2004). Focussing initially on an ideal configuration of a shear flow with a density jump (Miles 1957), Miles (1960) showed that the presence of a shear flow may lead to an enhancement of the energy transfer to the waves in turbulent shear flows. This scenario is based on the presence of a critical layer (Miles 1957) at the height z_c where the phase velocity of the waves matches the velocity $U_t(z_c)$. It is usually called the Miles instability. The Miles instability permits the transfer of energy from the mean flow to the wave if at the critical height z_c , the second derivative of U_t is negative. This instability is characterized by waves induced stress, where the Reynolds stresses $\tau = -\langle u'_x u'_x \rangle$ of the velocity fields are non-zero. A physical interpretation of the instability is given by Lighthill (1962). This mechanism is similar to the critical layer encountered in shear flow without inflection point (Drazin & Reid 2004), but it differs from the critical layer found in stratified flows, where the internal gravity wave gives its energy to the mean flow, even if the amplitude of the wave may increase due to the wave-action conservation (Sutherland 2010). Our measurements show that the mechanism of amplification operating in the dome shares some features with the Miles instability. Despite the difference in geometry between the framework of the Miles instability and our configuration, we use the theoretical result of the Miles instability, in the absence of theoretical prediction adapted to our case.

First, we look for the region of resonance where the typical phase velocity c_p and the tangential velocity U_t are equal. In figure 12(a), the velocity U_t is divided by the phase velocity $c_p = 2\text{cm/s}$ for the half plane of symmetry of the jet given by $x > 0$. The white curve is the mean interface $\langle h \rangle$. The closed dashed curve represents the contour where $U_t = c_p$: inside this region, the wave may propagate slower than the flow. The enclosed region appears for $|x| > 0.58b_d$ and ceases for $x \simeq b_d$. If the Miles instability is present, an increase of the disturbance energy must be seen through the action of the Reynolds stress (Lin 1954; Drazin & Reid 2004). The energy transfer between the mean flow and the waves is given by the production term $P(x, z) = \tau S_0$, with the large scale shear $S_0 = \partial_x \langle u_z \rangle + \partial_z \langle u_x \rangle$ and the Reynolds stress $\tau = -\langle u'_x u'_z \rangle$. The Miles instability must be associated with a positive production term in the region where $c_p > U_t$. The production term P is calculated for the run M3 (see table 1) and it is reported on figure 13. We observe that the production term is positive for $|x|$ larger than $0.1b_d$ and it becomes negative for $|x|$ in between $0.55b_d$ and $0.75b_d$, depending on the height. The transition between positive and negative production occurs in the region where $U_t \simeq c_p$ for $|x| = 0.58b_d$ (dashed curve figure 12(a)), suggesting the presence of a critical layer. The production term is non-zero above the interface, as expected from the Miles

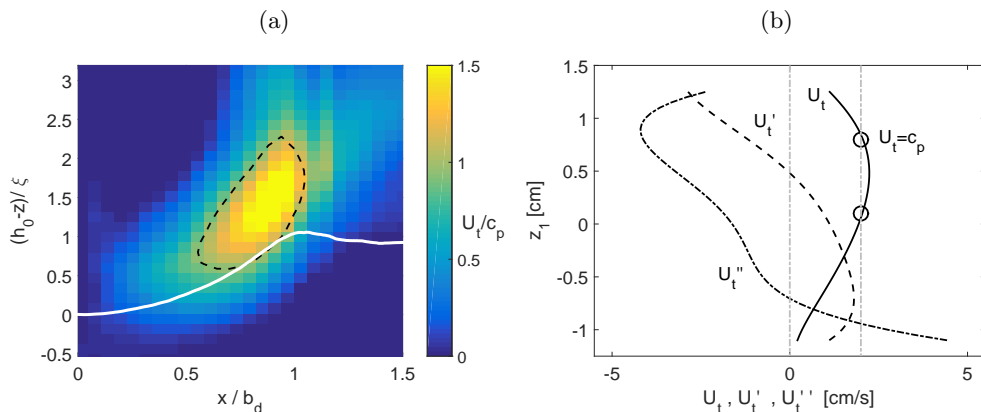


FIGURE 12. (a) Tangential velocity U_t divided by the phase velocity $c_p = 2 \text{ cm/s}$. The black dashed curve represents the contour where $U_t = 2 \text{ cm/s}$. The white curve corresponds to the interface. (b) Profile of the tangential velocity U_t corresponding to the abscissa $x = 0.7b_d$ extracted from figure 4(b). Its first U_t' and second U_t'' depth derivatives are represented respectively by dashed and dotted lines. The circles correspond to the points where the velocity is equal to c_p .

instability. The sign of the shear S_0 remaining constant for each side of the dome ($S_0 < 0$ for $x < 0$ and $S_0 > 0$ for $x > 0$), the variation of P is associated with a change of sign of the Reynolds stress τ . It is a classical property of the critical layer (Miles 1957; Drazin & Reid 2004). The relative phase between u_x' and u_z' varies abruptly across the critical layer where $U_t = c_p$, leading to a change of the sign of the production term (Lin 1954). The sign of P is also correlated to the variation of the height A_η of the waves (figure 10(a)). The height of the wave increases when P is positive and it decreases when P becomes negative. From the production term P and the kinetic energy of the wave $e = \langle u_x'^2 + u_z'^2 \rangle / 2$, an estimation of the energy transfer rate σ of the wave is possible with $\sigma = P / (2e)$. We report the maxima (heavy black line) and the minima (dashed black line) of the dimensionless energy transfer rate σT for all heights z in the dome as a function of x/b_d on figure 14. The positive energy transfer rate reaches the values $0.8T^{-1}$ at $x = 0.4b_d$ and the damping rate reaches the values $-0.95T^{-1}$ for $x = b_d$. We clearly observe that the waves are amplified, with $\sigma > 0$, in the central region and they are significantly damped outside, with $\sigma < 0$. The grey lines correspond to the abscissa $x = \pm 0.58b_d$ where the waves may propagate slower than the mean flow. Once again, the transition between amplification process and damping process occurs in the region where the waves cross the critical layer.

The calculation of the growth rate of the Miles instability is complex and an explicit formula exists only for idealized configurations (Miles 1957; Morland & Saffman 1993; Drazin & Reid 2004). The growth rate depends on properties of the mean flow at the critical layer and its calculation requires the knowledge of the amplitude of the initial neutral perturbation. It is out of reach of the present study and we will only focus on the sign of the growth rate in order to confirm the presence of the instability. The growth rate is given at leading order in ρ_1/ρ_2 (Miles 1957; Drazin & Reid 2004; Young & Wolfe 2014)

$$\sigma = -\frac{\pi}{2} \frac{\rho_1}{\rho_2} c_p \left(\frac{d^2 U_t}{dz_1^2} \right) \left(\frac{dU_t}{dz_1} \right)^{-1} \left| \frac{\phi_c}{\phi_s} \right|^2 \quad (4.3)$$

with $|\phi_c/\phi_s|$ the ratio of the streamfunction at the critical layer, which is especially

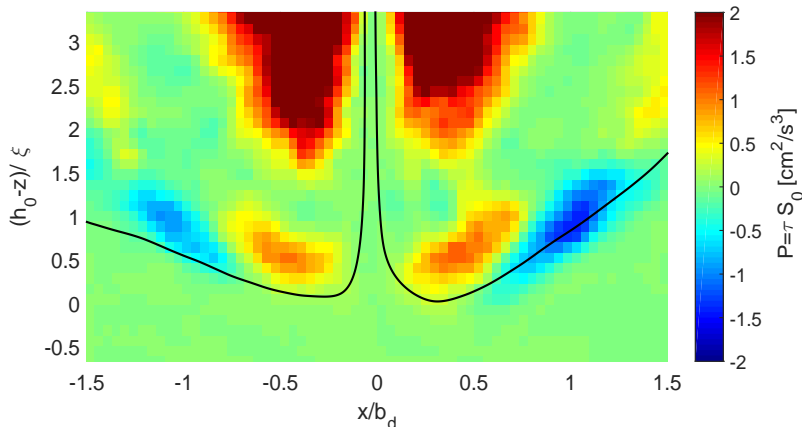


FIGURE 13. Production term $P(x, z) = \tau S_0$ with $\tau = -\langle u'_x u'_z \rangle$ the Reynolds stress and S_0 the large scale shear. The black curve corresponds to the streamline passing close to the stagnation point.

difficult to estimate. Considering wave-amplification, the growth rate may be interpreted as a energy transfer rate from the mean flow to the waves (Miles 1960). The criteria of instability requires that the second derivative of U_t must be negative. In figure 4(b), the profiles of U_t are concave, which suggests that $U_t'' = (d^2 U_t)/(dz_1^2)$ is negative. We verify this properties for the profile at $x = 0.7b_d$ (fifth profile starting from the left of figure 4), where $U_t = c_p$ for z_1 equal to 0.1 and 0.85cm. The first derivative U_t' and the second derivative U_t'' are reported on figure 12(b). The derivative U_t'' remains negative in the region where the wave can be in resonance with the mean flow. The derivative U_t' is positive for $z_1 < 0.5$ cm. The sign of the ratio U_t''/U_t' being negative, the mechanism of the Miles instability may amplify the wave. Our result shows that the amplification mechanism shares features with the Miles instability, suggesting the presence of a critical layer, that amplifies the waves generated by the eddies from the jet.

We have shown in the previous section that the waves are generated by the eddies of the jet and not by an instability. It could seem contradictory to the present section, which aims to demonstrate the presence of an instability. However, both mechanisms are complementary: the turbulence excites the waves and the instability amplifies them. It is a scenario similar to the ocean-wave generation mechanism. The opposite scenario may be addressed, i.e the waves are triggered by the instability and amplified by the turbulence. However, it is not very likely that the Miles instability may trigger a wave on a distance comparable to the half-wavelength. For the last point, Phillips (1957) has considered the wave-amplification by a resonance between the turbulent pressure field and the waves. By taking into account the presence of a critical layer, Miles (1960) has shown that this process is strongly enhanced by the Miles instability. Thus, once the wave is triggered, the energy transfer from the mean flow should be significantly larger than the energy coming from the turbulent fluctuations.

4.5. Wave breaking

We now focus on the wave breaking occurring in the region $0.6 < |x/b_d| < 1$. In this area, different elements may explain the wave breaking. First, we have shown that when the phase velocity becomes larger than the mean velocity, the negative Reynolds stress damps the wave due to the critical layer. Then, the profile of U_t becomes much

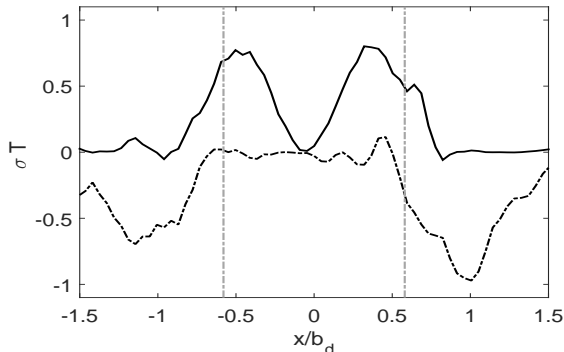


FIGURE 14. Maxima (heavy line) and minima (dashed line) of the dimensionless energy transfer rate $\sigma = P/(2E)$ rescaled by the wave-period T , where P is the production term and E the kinetic energy, for all heights z in the dome as a function of x/b_d . The grey lines correspond to the abscissa $x \pm 0.58b_d$ where the waves may propagate slower than the mean flow.

steeper for $|x| > 0.6b_d$ (figure 4(b)). The associated local Richardson numbers (insert in figure 5(b)) are of order unity in this region, which may lead to a destabilization of the wave by a shear-instability. Finally, the steepness of the wave, which is defined by the product of the wavenumber k_0 with the height A_η , becomes close to the critical steepness of the wave (Babanin 2011). We consider the maximum average height of the wave (dotted curve indexed by *total*, figure 10(a)), which reaches the values $A_\eta^{max} \simeq 0.56\xi$ with $\xi \simeq 0.8\text{cm}$, i.e. $A_\eta^{max} = 0.45\text{cm}$, for the run M2 (table 1). The maximum steepness based on the smallest wavenumber $k = 0.5k_0$, where $k_0 = 2\pi/b_d$ (run M2, see tab.1), is $kA_\eta^{max} \simeq 0.35$, a value in the range of wave-breaking criteria $kA_\eta^{max} \in [0.3 - 0.4]$ for ocean-waves (Babanin 2011). The damping, the shear and the large steepness of the wave may lead to the wave breaking. It is difficult to disentangle the different effects, which can of course interplay between each others (Banner & Song 2002).

After the breaking region just above the interface (figure 7(a) for $x \in [4, 6]\text{cm}$ and $h_0 - z \in [1, 3]\text{cm}$), we observe an area of mixed fluid with a relative density $\hat{\rho}$ varying between 0.4 and 0.2. It shows that the breaking has already induced mixing. Indeed, wave-breaking is believed to be the main mechanism of mixing at low Froude number (Fernando 1991; Fernando & Hunt 1996). The mixed fluid is then transported upstream, following the streamlines of the mean flow (figure 3). Figure 6(a) shows that the mixing continues at the frontier of the jet, where the turbulent intensity is expected to be important (List 1982). Due to the lateral entrainment of the jet (section 3.2), a part of the mixed fluid is directly injected inside the turbulent jet.

4.6. Remark on the length and time scales

We have studied the different properties of the generation, the amplification and the breaking of the waves in the previous sections. These different mechanisms take place on a distance, i.e. the width of the dome, comparable to the wavelength of the wave. In the framework of the Miles instability, the long-wavelength perturbations are the most unstable (Miles 1957; Morland & Saffman 1993; Drazin & Reid 2004). This mechanism could explain the observed large wavelengths in our confined geometry. From the lagragian point of view, the waves are generated and destroyed on time scales comparable to their period of oscillation. Figure 14 confirms that the evaluated energy transfer rate between the waves and the mean flow is close to the frequency of the wave.

Unlike classical studies of waves propagation, the times and length scales are not well decoupled, which is a limitation of the local study of the stability of the interface.

Our study shows that the wavelength, the frequency and the growth-rate of the waves are determined by the forcing and the amplification mechanisms. In section 4.4, we have shown that both mechanisms are not independent: the perturbations propagating toward the dome oscillate at the wave frequency. A possible explanation is the existence of a global mode, coupling the dynamics of the interface and the flow outside the dome. The limitation of our local study may be due to the interpretation of a global mode in term of local perturbations. More work is needed for the theoretical analysis of the observed results, but we think the basic physical processes are correctly described here.

5. A scaling law for the entrainment rate

5.1. The scaling law

In the previous sections, we have demonstrated that the erosion is related to the dynamics of gravity interfacial waves. We want to address in this section the scaling law for the erosion rate, given by equation 1.1, as a function of the Froude number based on our observations. Linden (1973), Cotel & Breidenthal (1996) and Shrinivas & Hunt (2014) have suggested different physical arguments for the scaling law, leading to $E_i \sim Fr_i^3$ for the two first authors and $E_i \sim Fr_i^2$ for the later authors for $Fr_i < 1$. These models have not considered mechanisms involving waves for the erosion process, except for a footnote (page 476) in Linden (1973) from Dr E. J. Hinch. Based on the data of Baines (1975) and Baines *et al.* (1993), the entrainment rate should follow a Fr_i^3 scaling law at low Froude number and a linear scaling law at large Froude number. The volumetric flux entrained across the interface Q_e (equation 1.1) varies with the vertical entrainment velocity u_e defined as the amount of fluid entrained per unit height per unit time (Linden 1973). The entrainment rate, defined in equation (1.1), varies with the ratio u_e/u_i (Cotel & Breidenthal 1996)

$$\frac{u_e}{u_i} \sim \frac{l_e f_e}{u_i} \quad (5.1)$$

where l_e and f_e are typical length and time associated with the erosion process and u_e the vertical velocity of the interface. As we consider waves amplified by an unstable mechanism, l_e is related to the relative length over which the amplification takes place, and f_e to the frequency of the wave-perturbation. We have shown that the waves are triggered by the eddies in the jet with time scale comparable to the buoyancy frequency, i.e. $f_e = \sqrt{g'/b_i}$. We choose the length l_e as the distance l travelled by the wave inside the dome minus the dome radius, i.e. $l_e = l - b_d$ (see fig.15(a)).

The waves exchange energy with the mean flow during the propagation along the distance l (section 4.4). Hence, all the steps leading to the breaking of the waves take place on this distance. The length $l_e = l - b_d$ corresponds to a “useful” length in the sense that for $Fr_i \rightarrow 0$, no distortion and no erosion are expected in our model. This mathematical regularisation prevents the divergence of E_i for $Fr_i \rightarrow 0$, a regime not considered here. Cotel *et al.* (1997) report a constant erosion rate E_i for $Fr_i < 0.14$, when the interface is almost flat. Our model quantifies the departure from this regime. Thus, we construct the length l_e , so that it corresponds to the additional length travelled by the wave, when the dome is deepening for a constant dome radius b_d . The infinitesimal length dl travelled by the wave on a interval dx is $dl = \sqrt{dz(x)^2 + dx^2}$ (figure 15(a)) and the useful length l_e is

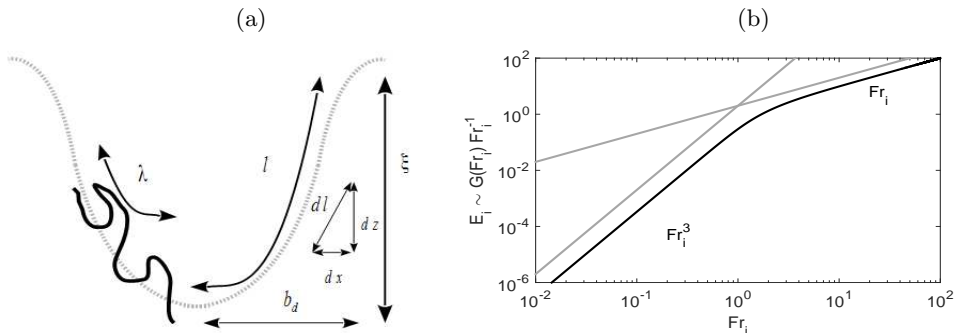


FIGURE 15. (a) Schematic and notation for the model of entrainment rate. (b) Entrainment rate as a function of the Froude number given by equation (5.10). The grey curves show the Fr_i^3 power law valid at low Froude number and the linear scaling Fr_i valid at large Froude numbers.

$$l_e = \int_{x=0}^{b_d} \left[\sqrt{\left(\frac{d\langle h \rangle}{dx}\right)^2 + 1} \right] dx - b_d \quad (5.2)$$

with $\langle h \rangle(x)$ the depth of the dome as a function of x . Our measurements show that $\langle h \rangle(x) = \xi(x/b_d)^2$, with ξ the depth of the dome. By using the change of variable $x = ub_d$, the integral becomes

$$l_e = b_d \int_0^{u=1} \left[\sqrt{(\epsilon u)^2 + 1} \right] du - b_d \quad (5.3)$$

with $\epsilon = \xi/(2b_d)$. The integration gives

$$l_e = \frac{b_d}{2} \left[\sqrt{(\epsilon)^2 + 1} + \frac{\sinh^{-1}(\epsilon)}{\epsilon} - 2 \right] \quad (5.4)$$

with \sinh^{-1} the inverse of the hyperbolic sinus. We assume that the dome radius b_d varies linearly with the radius of the jet b_i . An energy balance between the kinetic energy of mean flow and the potential energy stored in the dome shows that $\epsilon = \xi/(2b_d) \sim Fr_i^2$, confirmed by the measurements of Shy (1995). For low Froude number $Fr_i < 1$, ϵ tends to zero and the length l_e follows the asymptotic

$$\frac{l_e}{b_d} \sim \epsilon^2 \quad (5.5)$$

The model shows that the length l tends to b_d for $Fr_i \rightarrow 0$. At large Froude number with $\epsilon \gg 1$, we obtain

$$\frac{l_e}{b_i} \sim \epsilon \quad (5.6)$$

The two asymptotic behaviours are given by the function $G(Fr_i) = l_e/b_i$

$$G(Fr_i) = \frac{l_e}{b_i} \sim \begin{cases} \epsilon^2 \sim Fr_i^4 & \text{for } Fr_i \ll 1 \\ \epsilon \sim Fr_i^2 & \text{for } Fr_i \gg 1 \end{cases} \quad (5.7)$$

Finally, the entrainment rate is given by

$$E_i \sim \frac{l_e}{b_i} \frac{\sqrt{g' b_i}}{u_i} \sim Fr_i^{-1} G(Fr) \quad (5.8)$$

hence

$$E_i \sim \begin{cases} Fr_i^3 & \text{for } Fr_i \ll 1 \\ Fr_i & \text{for } Fr_i \gg 1 \end{cases} \quad (5.9)$$

Our model recovers both asymptotic behaviours as a function of the Froude number (figure 15(b)). We define the parametrization of the entrainment rate

$$E_i = \alpha Fr_i^{-1} G\left(\frac{\xi}{b_i}\right) \quad \text{with} \quad \frac{\xi}{b_i} = \beta Fr_i^2 \quad (5.10)$$

with (α, β) two real constants. The coefficient β characterizes the crossover point $Fr_t = \beta^{-1/2}$, where the scaling law varies from Fr_i^3 to Fr_i .

We now compare our model to the entrainment rate obtained in different processes of erosion (buoyant jets and plumes). We use figure 12(a) from Shrinivas & Hunt (2014) containing the measurements of Baines (1975) (triangles), Kumagai (1984) (squares), Baines *et al.* (1993) (crosses) and Lin & Linden (2005) (circles). We have reported the curve defined by equation (5.10) with $(\alpha, \beta) = (1.5, 0.45)$ in figure 16 (dotted curve). These parameters are determined by the best fitting of the experimental points of Baines (1975) (triangles), Baines *et al.* (1993) (crosses) and Lin & Linden (2005) (circles). The value of the coefficient β defines the crossover point occurring at $Fr_t = 1.49$. The agreement is good between the theory and the experimental data. To conclude, our model requires only one fitting amplitude parameter, here α , to fit the data both at low and large Froude number, once we have fixed the crossover point (given by β), unlike former models which require one parameter for each range.

5.2. Data of Kumagai

In figure 16, the data of Kumagai (1984) (upper branch) display a different trend relatively to the measurements of Baines (1975), Baines *et al.* (1993) and Lin & Linden (2005) (lower branch). The entrainment rate is approximatively one order of magnitude larger than the other measurements. The exponent n of the scaling law has been debated for small Froude numbers: Kumagai (1984) initially proposed $n = 3$ (dashed curve, figure 17), whereas Cardoso & Woods (1993) and Shrinivas & Hunt (2014) suggested $n = 2$ (dotted line, figure 17). The data being scattered, both models seem valid. Hence, the existence of the upper branch may be interpreted in two different ways. If n is equal to 2, two different physical mechanisms operate between the lower and the upper branch, as suggested in Shrinivas & Hunt (2015). If n is equal to 3, the mechanism is unchanged but the pre-factors in the equation (5.10), α and β , vary with the conditions of the experiments, for instance because of confinement.

The data of Kumagai (1984) suggest that the transition between the behaviour at small and large Froude number occurs earlier compared to the lower branch. We have reported some values of the entrainment rate as a function of the Froude number (black squares) from figure 12 of Kumagai (1984) in figure 17. We observe a transition around $Fr_t \in [0.25 - 0.35]$ in the upper branch (figure 17) whereas the lower branch is characterized by $Fr_t = 1.49$ (figure 16). We recall that the coefficient β in equation (5.10) determines the value of the transition $Fr_t = \beta^{-1/2}$. Hence, the entrainment rates measured by Kumagai

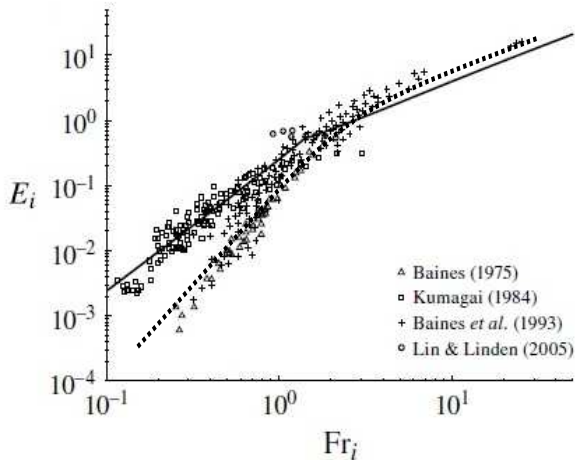


FIGURE 16. Modified figure from Shrinivas & Hunt (2014) (figure 12(a)). The dotted line corresponds to the scaling law defined by equation (5.10). The black line corresponds to the scaling law $E_i = 0.24Fr_i^2$ for small Froude numbers and $E_i = 0.42Fr_i$ at large Froude number, suggested by Shrinivas & Hunt (2014).

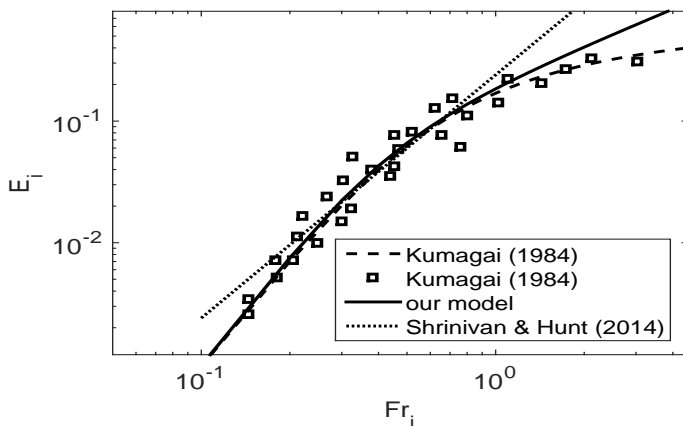


FIGURE 17. Erosion rate $E_i(Fr_i)$ (black squares) from figure 12 in Kumagai (1984). The dashed curve corresponds to the empirical model of Kumagai (1984). The dotted line is the scaling law from Shrinivas & Hunt (2014) with $E_i = 0.24Fr_i^2$. The heavy curve corresponds to the model given by (5.10) with $(\alpha, \beta) = (0.015, 14)$, associated with a crossover point at $Fr_t = 0.27$.

(1984) may differ from the ones of the lower branch because β and α are different. Three models are reported in figure 17: the dashed curve corresponds to the empirical model of Kumagai (1984), the dotted line is the scaling law $E_i = 0.24Fr_i^2$ from Shrinivas & Hunt (2014) and the heavy black curve is given by the equation (5.10) with $(\alpha, \beta) = (0.015, 14)$ with a crossover point at $Fr_t = 0.27$. Our model follows the model of Kumagai (1984) up to $Fr_i \simeq 1$. Once again, the set of data is not sufficient to determine which model is the best, even if we recover the empirical model of Kumagai (1984). However, our model

shows that one possible origin of the upper branch is a modification of the pre-factors between the experiments.

Our model is based on the deformation of the interface and when the interface is weakly deformed, the entrainment rate follows a scaling law Fr_i^3 for $Fr_i < Fr_t$. The coefficient β determines the transition between a weakly deformed interface, when the width of the dome is larger than its depth, and a strongly deformed interface, when the width is significantly smaller than the depth. This transition should depend on the confinement, but also on the nature of the jet (buoyant or not) or the time-dependence of the erosion. Hence, the scatter of the measurements may be explained by a modification of the pre-factors (α, β) , where β characterizes the efficiency of the plume to deform the interface. But again, the physics of the erosion, dominated by breaking interfacial waves excited by the turbulent fluctuations and amplified by the mean flow, may remain the same.

6. Conclusion

In the present paper, we have investigated the mechanism of entrainment by a turbulent jet impinging on a density interface with moderate Reynolds number and moderate Froude number. In this regime, the vortices coming from the jet are not able to deform significantly the interface via ballistic impacts, as commonly expected by previous model involving baroclinic turbulence inside the dome. Their role is reduced to trigger interfacial gravity waves. The main source of energy comes from the mean flow, which amplifies the perturbation of the interface by a mechanism of wave-induced stress. The sign of the Reynolds stress changes abruptly inside the dome, where the phase velocity of the wave and the mean velocity field are equal. These features suggest the presence of a resonance between the wave and the mean flow. Wave amplification leads to wave-breaking in the vicinity of the border of the impinged region. The induced mixing is responsible for the irreversible erosion of the interface.

Based on these physical observations, we have introduced a scaling law, which varies continuously from the Fr_i^3 to the Fr_i power law from small to large Froude numbers, in agreement with some of previous experimental measurements. Our model offers an alternative to Shrinivas & Hunt (2015): we suggest that the scatter of the measurements of the entrainment rate is rather due to a difference between the pre-factors of the scaling law rather than a modification of the exponents.

Our measurements are performed for Reynolds numbers below the mixing transition, i.e. $Re < 10^4$. It will be interesting to investigate the mechanism of erosion at low Froude number and larger Reynolds numbers ($Re > 10^4$), in order to verify if the present mechanism still operates or if others processes occur. For larger Reynolds numbers, the vortices impinging the stratification may be able to generate baroclinic vortices and turbulence at the interface, as suggested by Shy (1995). The model based on baroclinic effect, introduced by Shrinivas & Hunt (2014) and Shrinivas & Hunt (2015), could be then relevant.

Acknowledgements

The authors thank three anonymous referees for their comments and F. Duval (LIE, IRSN) and J.M. Ricaud (LIE, IRSN) for stimulating discussions. They acknowledge the support from the Institut de Radioprotection et de Sûreté Nucléaire and region PACA (France) under the APEX program 2015 (Project S2URF).

REFERENCES

- ALEXAKIS, A. 2009 Stratified shear flow instabilities at large Richardson numbers. *Physics of Fluids* **21** (5), 054108.
- BABANIN, A. 2011 *Breaking and dissipation of ocean surface waves*. Cambridge University Press.
- BAINES, W. D. 1975 Entrainment by a plume or jet at a density interface. *Journal of Fluid Mechanics* **68** (02), 309–320.
- BAINES, W. D., CORRIVEAU, A. F. & REEDMAN, T. J. 1993 Turbulent fountains in a closed chamber. *Journal of Fluid Mechanics* **255**, 621–646.
- BANNER, M. L. & SONG, J. B. 2002 On determining the onset and strength of breaking for deep water waves. part II: Influence of wind forcing and surface shear. *Journal of Physical Oceanography* **32** (9), 2559–2570.
- BREIDENTHAL, R. E. 1992 Entrainment at thin stratified interfaces: The effects of Schmidt, Richardson, and Reynolds numbers. *Physics of Fluids* **4** (10), 2141–2144.
- CARDOSO, S. S. S. & WOODS, A. W. 1993 Mixing by a turbulent plume in a confined stratified region. *Journal of Fluid Mechanics* **250**, 277–305.
- CHANDRASEKHAR, S. 1961 *Hydrodynamic and Hydromagnetic Stability*. Dover Publications.
- COTEL, A. J. & BREIDENTHAL, R. E. 1996 A model of stratified entrainment using vortex persistence. *Applied Scientific Research* **57** (3-4), 349–366.
- COTEL, A. J., GJESTVANG, J. A., RAMKHELAWAN, N. N. & BREIDENTHAL, R. E. 1997 Laboratory experiments of a jet impinging on a stratified interface. *Experiments in Fluids* **23** (2), 155–160.
- DIMOTAKIS, P. E. 2000 The mixing transition in turbulent flows. *Journal of Fluid Mechanics* **409**, 69–98.
- DRAZIN, P. G. & REID, W. H. 2004 *Hydrodynamic Stability*. Cambridge University Press.
- EZHOVA, E., CENEDESE, C. & BRANDT, L. 2016 Interaction between a vertical turbulent jet and a thermocline. *Journal of Physical Oceanography* **46** (11), 3415–3437.
- FERNANDO, H. J. S. 1991 Turbulent mixing in stratified fluids. *Annual Review of Fluid Mechanics* **23** (1), 455–493.
- FERNANDO, H. J. S. & HUNT, J. C. R. 1996 Some aspects of turbulence and mixing in stably stratified layers. *Dynamics of Atmospheres and Oceans* **23** (1), 35–62.
- FISCHER, H. B., LIST, J.E., KOH, C.R., IMBERGER, J. & BROOKS, N.H. 1979 *Mixing in inland and coastal waters*. Academic Press, San Diego (USA).
- HOLMBOE, J. 1962 On the behavior of symmetric waves in stratified shear layers. *Geophys. Publ* **24**, 67–113.
- HUSSEIN, H. J., CAPP, S. P. & GEORGE, W. K. 1994 Velocity measurements in a high-Reynolds-number, momentum-conserving, axisymmetric, turbulent jet. *Journal of Fluid Mechanics* **258**, 31–75.
- JANSSEN, P. 2004 *The interaction of ocean waves and wind*. Cambridge University Press.
- KHATTAB, I. S., BANDARKAR, F., FAKHREE, M. A. A. & JOUYBAN, A. 2012 Density, viscosity, and surface tension of water+ ethanol mixtures from 293 to 323K. *Korean Journal of Chemical Engineering* **29** (6), 812–817.
- KUMAGAI, M. 1984 Turbulent buoyant convection from a source in a confined two-layered region. *Journal of Fluid Mechanics* **147**, 105–131.
- LECOANET, D., LE BARS, M., BURNS, K. J., VASIL, G. M., BROWN, B. P., QUATAERT, E. & OISHI, J. S. 2015 Numerical simulations of internal wave generation by convection in water. *Physical Review E* **91** (6), 063016.
- LIGHTHILL, M. J. 1962 Physical interpretation of the mathematical theory of wave generation by wind. *Journal of Fluid Mechanics* **14** (03), 385–398.
- LIN, C. C. 1954 Some physical aspects of the stability of parallel flows. *Proceedings of the National Academy of Sciences of the United States of America* **40** (8), 741.
- LIN, Y. J. P. & LINDEN, P. F. 2005 The entrainment due to a turbulent fountain at a density interface. *Journal of Fluid Mechanics* **542**, 25–52.
- LINDEN, P. F. 1973 The interaction of a vortex ring with a sharp density interface: a model for turbulent entrainment. *Journal of Fluid Mechanics* **60** (03), 467–480.
- LIST, E. J. 1982 Turbulent jets and plumes. *Annual Review of Fluid Mechanics* **14** (1), 189–212.

- MEUNIER, P. & LEWEKE, T. 2003 Analysis and treatment of errors due to high velocity gradients in particle image velocimetry. *Experiments in Fluids* **35** (5), 408–421.
- MILES, J. W. 1957 On the generation of surface waves by shear flows. *Journal of Fluid Mechanics* **3** (02), 185–204.
- MILES, J. W. 1960 On the generation of surface waves by turbulent shear flows. *Journal of Fluid Mechanics* **7** (03), 469–478.
- MILES, J. W. 1961 On the stability of heterogeneous shear flows. *Journal of Fluid Mechanics* **10** (04), 496–508.
- MORLAND, L. C. & SAFFMAN, P. G. 1993 Effect of wind profile on the instability of wind blowing over water. *Journal of Fluid Mechanics* **252**, 383–398.
- PHILLIPS, O. M. 1957 On the generation of waves by turbulent wind. *Journal of Fluid Mechanics* **2** (05), 417–445.
- SHRINIVAS, A. B. & HUNT, G. R. 2014 Unconfined turbulent entrainment across density interfaces. *Journal of Fluid Mechanics* **757**, 573–598.
- SHRINIVAS, A. B. & HUNT, G. R. 2015 Confined turbulent entrainment across density interfaces. *Journal of Fluid Mechanics* **779**, 116–143.
- SHY, S. S. 1995 Mixing dynamics of jet interaction with a sharp density interface. *Experimental Thermal and Fluid Science* **10** (3), 355–369.
- STRANG, E. J. & FERNANDO, H. J. S. 2001 Entrainment and mixing in stratified shear flows. *Journal of Fluid Mechanics* **428**, 349–386.
- SUTHERLAND, B. 2010 *Internal Gravity Waves*. Cambridge University Press.
- WOODWARD, P. R., HERWIG, F. & LIN, P.-H. 2014 Hydrodynamic simulations of h entrainment at the top of he-shell flash convection. *The Astrophysical Journal* **798** (1), 49.
- WYGNANSKI, I. & FIEDLER, H. 1969 Some measurements in the self-preserving jet. *Journal of Fluid Mechanics* **38** (03), 577–612.
- YOUNG, W. R. & WOLFE, C. L. 2014 Generation of surface waves by shear-flow instability. *Journal of Fluid Mechanics* **739**, 276–307.
- YULE, A. J. 1978 Large-scale structure in the mixing layer of a round jet. *Journal of Fluid Mechanics* **89** (03), 413–432.